

Wave propagation in a model artery

Pierre Chantelot,¹ Alexandre Delory,² Claire Prada,¹ and Fabrice lemoult¹

¹*Institut Langevin, ESPCI Paris, Université PSL, CNRS, 75005 Paris*

²*ENS de Lyon, CNRS, LPENSL, UMR 5672, Lyon cedex 07, France*

(Dated: July 24, 2025)

Fluid filled pipes are ubiquitous in both man-made constructions and living organisms. In the latter, biological pipes, such as arteries, have unique properties as their walls are made of soft, incompressible, highly deformable materials. In this article, we experimentally investigate wave propagation in a model artery: an elastomer strip coupled to a rigid water channel. We measure out-of-plane waves using synthetic Schlieren imaging, and evidence a single dispersive mode which resembles the pulse wave excited by the heartbeat. By imposing an hydrostatic pressure difference, we reveal the strong influence of pre-stress on the dispersion of this wave. Using a model based on the acoustoelastic theory accounting for the material rheology and for the large static deformation of the strip, we demonstrate that the imposed pressure affects wave propagation through an interplay between stretching, orthogonal to the propagation direction, and curvature-induced rigidity. We finally highlight the relevance of our results in the biological setting, by discussing the determination of the arterial wall's material properties from pulse wave velocity measurements in the presence of pre-stress.

I. INTRODUCTION

The mechanical properties of cells, tissues, and organs are intimately tied to their physiological functions [1]. As a result, pathologies are often associated with alterations of the mechanical behavior of tissues: for example, alveolar lung disease is linked to a reduction of tissue shear modulus [2], and tumor cells are significantly stiffer than healthy ones [3]. Developing tools to probe the material properties of biological tissues *in vivo* is thus crucial to improve diagnosis. In the case of medical imaging, the development of shear wave elastography has shown that monitoring the propagation of elastic waves allows to quantitatively assess material properties [4, 5]. More generally, relating the velocity of elastic waves to the medium characteristics is relevant to a broad scope of applications ranging from non-destructive testing in industry [6, 7] to geophysics imaging [8].

Here, we focus on the link between the propagation of elastic waves in arteries and the stiffness of the arterial wall, a widely used marker of cardiovascular risk [9, 10]. An elastic wave is naturally excited as the heart beats and travels along the arterial tree, as first described by Young [11]. Locally measuring the propagation of this wave, called the pulse wave, and estimating the corresponding tissue elasticity constitutes the medical gold standard [12, 13]. The tissue stiffness is usually inferred from the Moens-Korteweg formula [14, 15], assuming a breathing motion and that the wave speed is set by an interplay between the linear elastic response of the wall and blood inertia.

This approach captures the essential physics of pulse wave propagation, but it fails to account for several clinical observations. It does not recognize that multiple modes are excited by the heartbeat, as demonstrated by the recent *in vivo* observation of an arterial flexion wave [16, 17]. It ignores that the pulse wave velocity is altered by pre-stress: variations of the mean blood pressure affect

the pulse wave velocity [18–20], and waves generated during elastography measurements are sensitive to the large transient deformations occurring during the cardiac cycle [21, 22]. The pulse wave thus probes the incremental stiffness of the arterial wall [23]. Additionally, elastography data highlight that wave guiding and viscoelastic material properties also influence wave propagation in arteries [21, 24–26].

Acknowledging these limitations, a rich literature builds upon the seminal work of Moens and Korteweg, addressing the finite deformations of tubes [27, 28], the material non-linearity of the arterial wall [29, 30], the influence of wave guiding and viscoelasticity [21, 26], and the role of pre-stress on wave propagation in fluid-loaded plates and tubes [22, 31–33]. In this article, we aim to integrate all these aspects into a comprehensive model that can be quantitatively compared with experimental data, ultimately allowing an accurate assessment of the arterial wall's material properties.

We first describe the guided waves that propagate in soft elastic tubes filled and surrounded by fluid, and provide analytical long-wavelength approximations for the propagation speed of the breathing and flexion modes observed *in vivo* (section II). Next, we introduce our experiment which consists in a square rigid conduit closed by an elastomer wall. This minimal artery phantom allows to successfully isolate a single mode resembling the breathing mode associated to the pulse wave. We impose a static fluid pressure, creating pre-stress, and highlight its influence on the dispersion relation of the breathing mode (section III). In section IV, we perform dedicated experiments, conducted in the absence of fluid coupling, to evidence how transversal stretching and curvature-induced rigidity combine through the deflection of the soft wall. We quantify the influence of pre-stress in a semi-analytical model, based on the acoustoelastic theory, that accounts for wave guiding, viscoelasticity, geometrical and material non-linearities. In section V, we

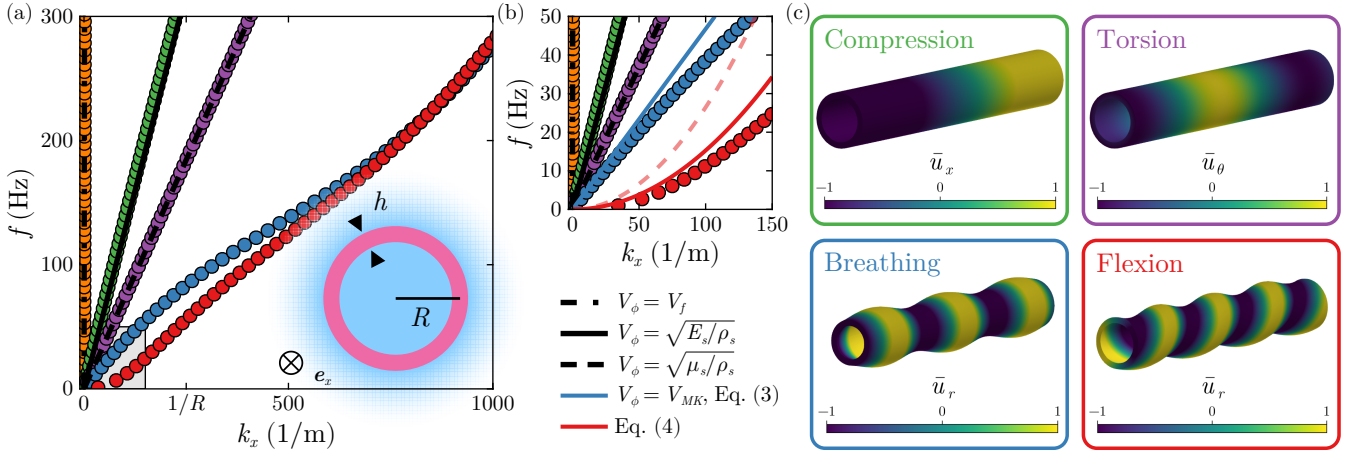


FIG. 1. (a) Dispersion relation of the axial waves propagating along a water filled incompressible elastic pipe ($\mu_s = 23$ kPa, $\rho_s = 1070$ kg m $^{-3}$) with radius $R = 4$ mm and thickness $h = 1$ mm surrounded by an infinite water medium. We represent only the six lowest order fluid (orange), compression (green), torsion (purple), breathing (blue), and flexion (red) modes. (b) Zoom of (a) in the small wavenumber limit, $k_x R \ll 1$ (greyed region), where one dimensional models successfully capture the dispersion of axial waves. (c) Displacement fields at 100 Hz for the solid zero order modes identified in (a), where the color code corresponds to the main component of the normalized displacement field for each mode.

tackle fluid coupling in the short and long-wavelength limits relevant to shear wave elastography and natural pulse wave propagation, respectively. Finally, we discuss the relevance of our results in inferring material properties from wave velocity measurements, with the aim of going beyond the determination of incremental elastic moduli (section VI).

II. AXIAL WAVES IN A SOFT PIPE

We consider a water-filled isotropic elastic tube with radius R , thickness h , density ρ_s , shear and longitudinal wave velocities, V_T and V_L respectively. The tube is immersed in an infinite water medium (density $\rho_f = 1000$ kg m $^{-3}$ and speed of sound $V_f = 1500$ m s $^{-1}$), as sketched in the inset of figure 1(a). Given this geometry, we focus on computing the dispersion relation of guided waves propagating along the direction of the pipe. Our aims are (i) to relate these results to *in vivo* observations of wave propagation in blood vessels, and (ii) to assess the ability of long-wavelength models to predict the relation between the tube wall stiffness and the pulse wave velocity.

A. Three-dimensional model

The displacement field \mathbf{u} in the inner fluid domain and in the tube wall satisfies the three-dimensional elastodynamics equation,

$$\nabla \cdot (\mathbf{C}_i : \nabla \mathbf{u}) = \rho_i \ddot{\mathbf{u}}, \quad (1)$$

where \mathbf{C} is the fourth-order elasticity tensor, and the subscript i denotes fluid (f) or solid (s) material proper-

ties (note that we model the fluid as an isotropic elastic solid with $V_L = V_f$ and $V_T/V_f \approx 10^{-9}$). The inner fluid and the elastic wall are coupled at the inner tube surface ($r = R - h/2$) by imposing the continuity of both the normal traction and the normal displacement. The presence of the surrounding fluid is taken into account in the boundary condition for the normal stress at the outer surface of the tube,

$$\mathbf{e}_r \cdot (\mathbf{C} : \nabla \mathbf{u})|_{r=R+h/2} = \frac{\rho_f \omega^2}{\gamma} \frac{H_m(\gamma r)}{H'_m(\gamma r)} u_r \mathbf{e}_r, \quad (2)$$

where H_m is the Hankel function of the first kind of order m , and $\gamma = \sqrt{k_f^2 - k_x^2}$ with k_f the wavenumber in the fluid, and k_x the axial projection of the wavenumber \mathbf{k} in the pipe [34, 35]. After inserting the displacement ansatz, $\mathbf{u} = \mathbf{u}(k_x, r, m, \omega) e^{i(k_x x + m\theta - \omega t)}$, the dispersion relation $k_x(\omega)$ is given by non-trivial solutions of the system of equations (1–2). Solutions to similar systems, where equation (1) is replaced by equations of motion derived from thin or thick shell theory, have been obtained by finding the zeroes of a transcendental equation [36–38]. Here, we use a semi-analytical approach that consists in discretizing the problem in the radial direction using the spectral collocation method [39–41]. The dispersion relation is obtained as the solution (k_x, \mathbf{u}) to an algebraic eigenvalue problem which incorporates an approximate boundary condition at the tube outer surface. This solution is then iteratively refined to fulfill the exact boundary condition given in equation (2) [35]. We emphasize that this approach enables us to find complex wavenumbers k_x while keeping ω real, which is key to modeling viscoelastic media. Our implementation, adapted from [35, 42], is detailed and available in [43].

B. Dispersion relation

For the sake of concreteness, we now consider a tube with dimensions similar to that of the carotid artery ($R = 4$ mm and $h = 1$ mm), and with material properties characteristic of a soft elastomer ($V_T = 4.6$ m s⁻¹ and $V_L = 1000$ m s⁻¹). The dispersion relations computed for this set of parameters, considering only the lowest order modes for $m = 0$ and $m = \pm 1$, are shown in figure 1(a). Six modes propagate in the low-frequency regime: the fluid mode (orange), the compression mode (green dots), the torsion mode (purple dots), the breathing mode (blue dots), and two degenerated flexion modes (red dots). The fluid mode, which is not associated to wall motion, as well as the compression and torsion modes, which displacement fields are predominantly polarized in the axial and azimuthal direction respectively (figure 1c), are barely observable *in vivo*. Therefore, we focus on the breathing and flexion modes, which have both been observed *in vivo* [16], thanks to the radial nature of their displacement field (figure 1c). When $k_x R \gg 1$, these two modes merge and, in the frequency range relevant to shear wave elastography that is typically from 100 Hz to 1000 Hz, both modes are dispersive indicating that waveguiding must be taken into account when analyzing such experiments [21, 24]. In the long-wavelength limit ($k_x R \ll 1$), the two modes display markedly different behaviors (figure 1b), that we now model and link to the arterial wall material properties.

C. Long-wavelength approximations for the breathing and flexion modes

In the long-wavelength limit, the breathing mode, classically associated to the pulse wave, propagates at a constant velocity. This wave speed can be related to the material properties using the Moens-Korteweg formula [14, 15]. We recall here the main steps of the derivation of this formula to evidence the physics of pulse wave propagation. Using mass and momentum conservation in the fluid contained inside the tube, the speed of a pressure disturbance in the fluid can be expressed as $V_b = \sqrt{A/(\rho_f \partial A / \partial P)}$, where A is the area of the fluid section, and P the pressure [44]. The response of the tube wall to an internal pressure increase dP can be derived by expressing the hoop stress using Laplace law for $h \ll R$, and using Hooke's law assuming plane membrane stress in the wall, giving $dPR/h = E_s dR/R$, where E_s is the Young modulus. Combining the two above relations yields the Moens-Korteweg formula,

$$V_{MK} = \sqrt{\frac{E_s h}{2\rho_f R}}, \quad (3)$$

which evidences that the breathing mode involves both the elasticity of the tube wall and the inertia of the fluid, that is much larger than that of the solid for thin tubes. It

is also worth noticing that, at first-order, the breathing mode velocity is not affected by the surrounding fluid, as evidenced here by the good agreement between the simulated dispersion and equation (3) (solid blue line in figure 1b).

In contrast, the flexion mode is dispersive for $k_x R \ll 1$, with a quadratic evolution $\omega \propto k_x^2$, characteristic of bending. In the case of a fluid-filled tube, this behavior can be captured by a one-dimensional model [17, 45]. The dynamics in the long-wavelength limit are described by an Euler-Bernoulli beam equation, $E_s I \partial^4 u_r / \partial x^4 + \rho_s A \ddot{u}_r = 0$, where I is the second moment of area and A is the beam cross-section [46]. After inserting the displacement ansatz, we get the dispersion relation $\omega = \sqrt{E_s I / (\rho_s A)} k_x^2$. This dispersion relation can be modified to take into account the presence of the inner fluid by recognizing that, similarly as for the breathing mode, the inertia of the fluid ($\rho_f \pi R^2$) dominates when $h \ll R$, yielding $\omega = \sqrt{E_s R h / \rho_f} k_x^2$ [17, 45]. Unlike for the breathing mode, this prediction (light red dashed line in figure 1b) does not satisfactorily describe the computed dispersion relation, highlighting the influence of the surrounding fluid. We incorporate this effect in the one-dimensional model by adding the load from the outer fluid to the beam equation. This load is the azimuthal integral of the pressure, given by equation (2) with $m = 1$, on the outer tube surface. We further simplify equation (2) upon noticing that the flexural wave velocity is much slower than that of sound waves in water, indicating that only evanescent waves exist in the outer fluid, *i.e.* $\gamma \approx i k_x$. Finally, we obtain the long-wavelength dispersion relation by performing asymptotic expansions of the Hankel functions,

$$\omega = \sqrt{\frac{E_s R h}{3\rho_f}} k_x^2, \quad (4)$$

that we represent with a red solid line in figure 1(b), and that convincingly fits our data for $k_x R \ll 1$. We point out that the influence of the surrounding fluid appears as an added mass effect here, multiplying by a factor three the mass of fluid set in motion compared to the case with inner fluid only.

Having identified the different modes of wave propagation in arteries, and established the link between the wave velocity and material properties in the long-wavelength limit for the modes observed *in vivo*, we perform experiments with the goal to reproduce the physics of the breathing mode.

III. A MINIMAL ARTERY PHANTOM

We design an experimental platform that allows to monitor breathing waves and investigate the parameters that influence their propagation properties, while being free of the compression, torsion and flexion modes that propagate along a tube.

A. Experimental setup and procedure

We build a deformable conduit by clamping a soft elastomer strip with thickness $h_0 = 770 \mu\text{m}$, to the top of a square section, rigid, open Plexiglas channel with dimensions $58 \text{ cm} \times 1 \text{ cm} \times 1 \text{ cm}$ (figure 2a). We choose to make the deformable wall from a silicone elastomer, Ecoflex OO-30 (Smooth On), as it shares the low shear modulus, on the order of 10 kPa, and the incompressible nature of biological tissues. Ecoflex OO-30 exhibits an hyperelastic behavior that we describe using the compressible Mooney-Rivlin model [47, 48] which involves two material parameters $\mu_0 = 23 \text{ kPa}$ and $\alpha = 0.29$. These values were taken from tensile tests conducted in a previous work [49]. Having discussed the response of this elastomer to static strain, we focus on its viscoelastic behavior. The shear modulus μ_s is both complex and frequency dependent, and its evolution is well captured by a fractional Kelvin-Voigt model [50, 51], $\mu_s = \mu_0 (1 + (i\omega\tau)^n)$, where $\tau = 330 \mu\text{s}$ and $n = 0.32$ were determined from oscillatory rheological measurements [49, 52]. The joint effects of pre-stress [53, 54] and viscoelasticity [55] are implemented in a modified elasticity tensor \mathbf{C}^0 which describes the elastomer response for incremental motions superposed on a large static deformation, as detailed in appendix A.

We fill the deformable conduit with water and connect it to a water column. Its height can be adjusted to impose a static pressure difference $\Delta P = \rho_f g \Delta H$ (where $g = 9.81 \text{ ms}^{-2}$ is the gravitational acceleration) between the channel and the ambient. This pressure difference, that we vary between 0 Pa and 2900 Pa, creates a finite deflection of the deformable wall's midline, $\delta(z)$.

After this static pre-stress is applied, a shaker drives a point-like source in the \mathbf{e}_y direction, creating small amplitude waves. The source generates a chirp signal with an instantaneous frequency varying from 1 Hz to 400 Hz in one second, and a CCD camera records images from the top at a frame rate of 800 Hz. The out-of-plane incremental displacement of the soft strip, $u_y(x, z, t)$, induces by refraction a deformation of the pattern placed below the conduit, allowing the use of a synthetic Schlieren imaging method [56] to retrieve the displacement field. As the usual checkerboard pattern would suffer from a large deformation caused by the static deflection of the elastomer, we use a line pattern oriented in the \mathbf{e}_z direction.

B. Dispersion relation

From these measurements, we first compute the monochromatic displacement field $u_y(x, z, f)$ by performing a Fourier transform in time for two imposed pressures $\Delta P = 0 \text{ Pa}$ and $\Delta P = 1500 \text{ Pa}$. The displacement average along the \mathbf{e}_z direction is represented in figure 2b for $f = 50 \text{ Hz}$ and $f = 150 \text{ Hz}$. We observe the propagation of a single mode, corresponding to flexural motion of the strip. These displacement profiles already show the influ-

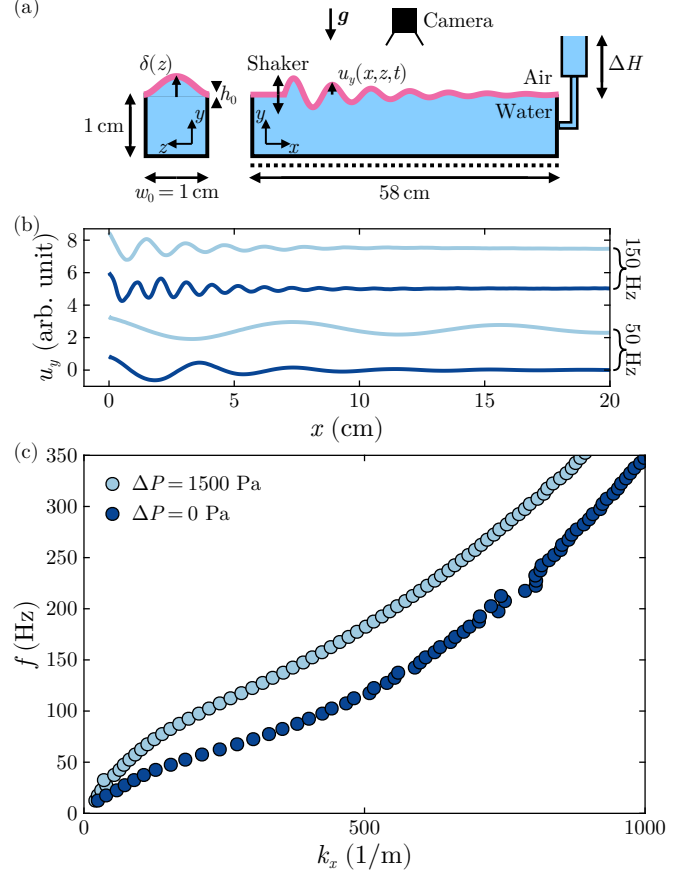


FIG. 2. (a) A soft compartment consisting of an elastomer strip ($h_0 = 1 \text{ mm}$, $w_0 = 1 \text{ cm}$) clamped to a rectangular water channel ($58 \text{ cm} \times 1 \text{ cm} \times 1 \text{ cm}$) is subjected to a pressure difference $\Delta P = \rho_f g \Delta H$, that induces a large deflection of the soft wall $\delta(z)$. We generate waves in the strip using a shaker, and measure the out-of-plane displacement field, $u_y(x, z, t)$, associated to wave propagation using Synthetic Schlieren imaging. (b) Out-of-plane displacement field averaged along the z direction for two frequencies: $f = 50 \text{ Hz}$ and $f = 150 \text{ Hz}$; and two imposed pressure differences: $\Delta P = 0 \text{ Pa}$ and $\Delta P = 1500 \text{ Pa}$. (c) Dispersion relations of the zero order mode for $\Delta P = 0 \text{ Pa}$ and $\Delta P = 1500 \text{ Pa}$. The mode dispersion closely resembles that of the breathing mode in a fluid-filled tube and is highly sensitive to ΔP .

ence of pre-stress. For both frequencies, the wavelength and the attenuation distance increase with ΔP . This highlights the interplay between the strain on the strip, induced by the hydrostatic pressure, and the viscoelasticity.

We then perform a spatial Fourier transform. By extracting maxima for each frequency in the (k_x, f) plane, we retrieve the dispersion relation of the guided axial waves. We show the result of this analysis for $\Delta P = 0 \text{ Pa}$ (dark blue) and $\Delta P = 1500 \text{ Pa}$ (light blue) in figure 2(c). The dispersion of axial waves is similar to that of the breathing mode in a fluid-filled tube (figure 1a), with a linear behavior at low frequency, followed by an inflection point and a parabolic shape as f increases. This

indicates that we have designed a model experiment that qualitatively reproduces the breathing mode dispersion, and is easier to study as we eliminated the compression, torsion and flexion modes. Figure 2(c) also highlights the sensitivity of the dispersion relation on ΔP , both in the non-dispersive, long-wavelength regime relevant to the determination of the Moens-Korteweg velocity (equation 3), and in the dispersive regime relevant to elastography.

We now focus on the impact of pre-stress on the dispersion of axial waves in both regimes.

IV. INFLUENCE OF PRE-STRESS

Applying a pressure difference ΔP leads to an initial out-of-plane deflection $\delta(z)$ (figure 1a). This static deformation both induces a transversal stretching of the strip, known to affect the dispersion of in-plane modes [49], and creates curvature, which enhances the static rigidity of shells [57–59]. To disentangle the influence of these two effects on the dispersion relation of the out-of-plane mode, we perform independent measurements, by imposing either an in-plane transversal stretch or a constant curvature. We then combine these two effects by applying a pressure difference ΔP using air as a fluid, allowing to neglect the fluid coupling. This step by step approach empowers us to propose a model that takes into account the influence of both stretching and curvature on waves propagating in pressurized soft conduits.

A. Transversal stretching of the strip

We clamp the soft elastomer strip (with width w_0 and thickness h_0) along its long edges, and impose an in-plane transversal stretch by adjusting the distance between the clamps $w = \lambda_z w_0$, where λ_z is the transversal stretch ratio (figure 3a). The boundary conditions prevent axial strain, so that the axial stretch ratio is one and, in the incompressible limit, the strip thickness is reduced by a factor $1/\lambda_z$. We identify a pure shear, homogeneous deformation whose deformation gradient \mathbf{F} is represented in figure 3(a). We then excite small amplitude out-of-plane waves in the strip as in section III. This time, as there is no water under the strip, the pattern deformation caused by refraction is minimal and we use a different technique to detect the out-of-plane displacement. A CCD camera records the deflection of a laser sheet projected in oblique incidence on the strip with an acquisition frequency of 800 Hz. The out-of-plane displacement $u_y(x, t)$ is directly proportional to the in-plane deflection of the laser line, which we extract from the images. We then obtain the dispersion relation of axial out-of-plane waves by performing the two-dimensional Fourier transform of $u_y(x, t)$ and extract maxima in the (k_x, f) plane.

We show in figure 3(b) the dispersion relation for three imposed values of λ_z (filled circles). Strikingly, we do not observe the non-dispersive low-wavenumber regime evi-

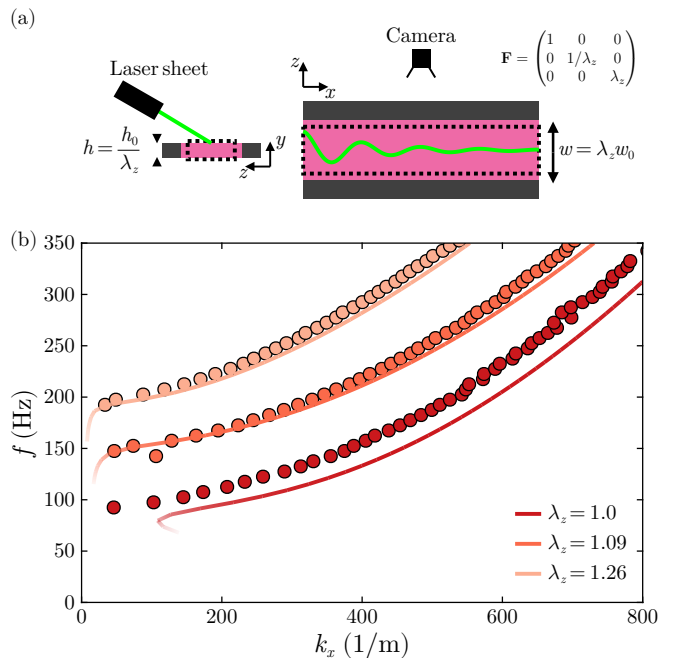


FIG. 3. (a) A soft strip, clamped along its edges, is subjected to an elongation in the \mathbf{e}_z direction. Elastic waves are generated using a shaker for three imposed values of the stretch ratio λ_z , and we extract the strip out-of-plane displacement $u_y(x, t)$ by recording the in-plane motion of a laser sheet in oblique incidence. (b) Dispersion curves of the lowest order flexion mode propagating in the strip for $\lambda_z = 1.0$, 1.09, and 1.26. The solid lines are predictions, obtained without fitting parameters, whose transparency renders the ratio $\text{Im}(k_x)/|k_x|$.

denced in figure 2(c). Indeed, this regime arises from an hybridization between the fundamental mode of the fluid waveguide and the flexion mode of the strip (as detailed in section V). Instead, the dispersion relations have a parabolic shape, and exhibit cutoff frequencies, originating in the clamped boundary condition along the lateral edges. Imposing a transversal stretch ($\lambda_z > 1$), shifts the dispersion curves upwards, indicating that tension orthogonal to the direction of propagation stiffens the strip. Yet, the propagation remains dispersive, unlike in the string-like regime reached when tension is applied along the principal direction of a beam [49]. We also observe that the dispersion relation obtained in figure 2(c) when imposing $\Delta P = 0$ Pa in the water channel is shifted downwards compared to that for $\lambda_z = 1.0$ when there is no channel at all, suggesting that the influence of water coupling partly originates from an added mass effect.

We model the influence of in-plane stretch using the acoustoelastic theory [53, 54], which describes incremental motions superimposed on a large deformation. We replace the elasticity tensor \mathbf{C} in equation (1) by the modified elasticity tensor $\mathbf{C}^0(\lambda_z, \omega)$, which incorporates both the effects of pre-stress and of viscoelasticity [55]. We solve this equation, where \mathbf{u} now stands for the incremental displacement, with boundary conditions of vanish-

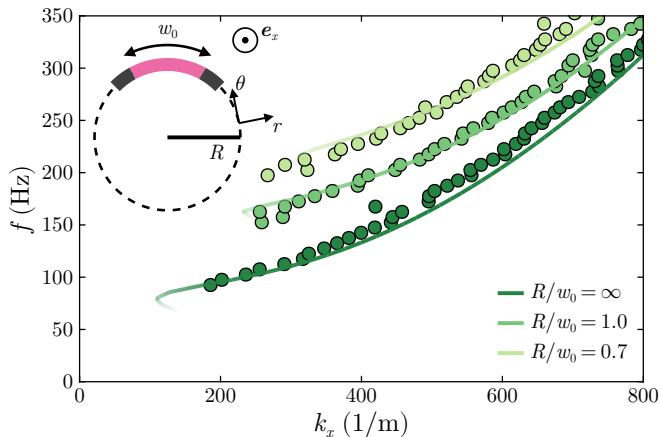


FIG. 4. Dispersion curves of the lowest order flexural mode propagating in clamped curved strips with normalized radius of curvature $R/w_0 = \infty, 1.0$, and 0.7 . The solid lines are predictions obtained without fitting parameters whose transparency renders the ratio $\text{Im}(k_x)/|k_x|$.

ing incremental traction at the free surfaces ($y = \pm h/2$, where $h = h_0/\lambda_z$), and zero incremental displacement at the clamped edges ($z = \pm w/2$). We use a solution procedure analogue to that detailed in section II with the displacement form taken as $\mathbf{u} = \mathbf{u}(k_x, y, z, \omega)e^{i(k_x x - \omega t)}$, and derivatives discretized in the y and z directions. Our implementation is identical to that of [60], and is available in [43]. The predictions (solid lines) are in satisfying agreement with our measurements (filled circles) for the three values of λ_z (figure 3b), suggesting that the modified elasticity tensor successfully captures the influence of the transversal stretch. We note that the agreement is not as good for $\lambda_z = 1.0$, revealing the experimental difficulty in ensuring a stress free reference configuration. We also encode the ratio of the imaginary part to the absolute value of the wavenumber in the transparency of the prediction lines, showing that stretching facilitates wave propagation at small wavenumbers, in agreement with the increase of the attenuation distance with pressure reported in figure 2(b). It highlights that accounting for the viscoelastic properties of the soft elastomer is crucial to obtaining quantitative agreement.

B. Strip curvature

We now investigate the influence of curvature on the propagation of out-of-plane waves. To this end, we design and build supports in order to impose a curvature R to the clamped strip while ensuring that its mid-surface is not stretched, as sketched in the inset of figure 4. Bending the strip into a cylindrical shape creates both transversal stretching and compression, that is in the direction \mathbf{e}_θ as it is now natural to use cylindrical coordinates. The maximal value of the stretch ratio in the azimuthal direction can be geometrically estimated as

$\lambda_\theta = 1 + h_0/(2R)$ so that, as $h_0 \ll R$, we assume in the following that the curved strip is stress free. As in section IV A, we use the laser sheet to measure the dispersion relation of axial waves for three imposed radii of curvature R (filled circles in figure 4). The frequency-wavenumber curves retain their parabolic shape but the cutoff frequency increases as R decreases, and the whole dispersion relation is shifted upwards. It appears that the curvature-induced rigidity effect identified in static indentation tests [57–59] carries over to the first axial flexion mode. Qualitatively, this stiffening can be understood using Gauss’ *Theorema Egregium* [61]: the deformation associated to the propagation of axial flexion waves on the curved strip is a non-isometric transformation. It thus generates in-plane stresses which act to rigidify the strip, as evidenced in section IV A.

We include curvature in our model by solving the elastodynamic equation in a cylindrical geometry, performing the discretization on r and θ , with the same boundary conditions as in IV A (details of the implementation are given in [43]). We emphasize here that, as the curved strip is assumed to be stress free, the modified elasticity tensor $\mathbf{C}^0(\lambda_\theta = 1, \omega)$ only accounts for the rheological behavior of the elastomer. The computed dispersion relations of the first flexion mode (solid lines in figure 4) are in excellent agreement with our experimental measurements, validating a posteriori the hypothesis of a stress free strip.

C. Imposed pressure: combining stretching and curvature

Having identified and modeled the respective influence of stretch and curvature on the bending mode, we explore their combined effect when imposing a pressure difference $\Delta P > 0$. In order to single out the influence of pre-stress from that of fluid coupling, we use air instead of water pressure in the deformable conduit. We insert a rigid vertical cylinder between the water column and the fluid waveguide (inset of figure 5a). This chamber allows water to act as a piston, compressing air in the waveguide with a pressure controlled by the height difference between the water in the column and in the intermediate chamber. In this configuration, we use the same experimental technique as in IV A to obtain the dispersion relations of axial out-of-plane waves for four values of ΔP , and represent them in figure 5(a). Unlike for a water filled conduit, the dispersion relations exhibit a parabolic shape and a cutoff frequency, highlighting the need of a strong coupling to observe an hybridization between the dispersion relation of the fluid waveguide and that of the strip. The curves are shifted upwards when increasing ΔP , as expected from the combined influence of tension and curvature that work together to stiffen the deformable wall.

The first step to model the influence of pressure on the dispersion relation is to link ΔP to the stretch and cur-

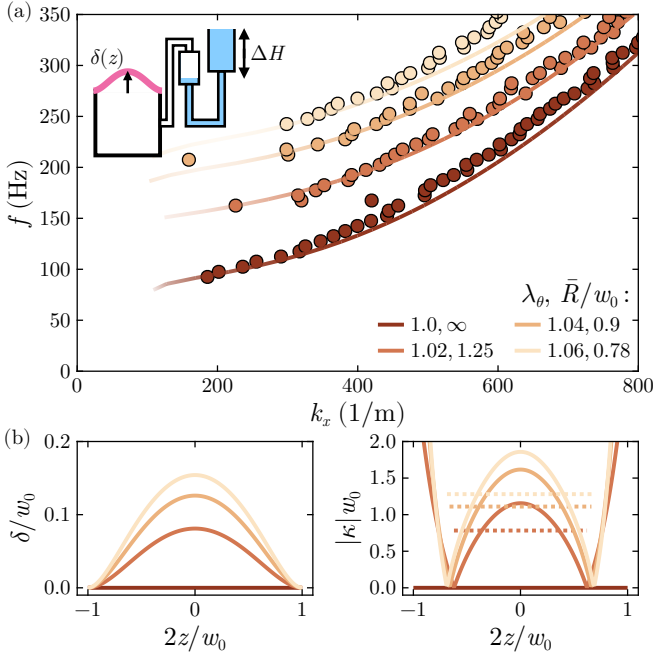


FIG. 5. (a) Dispersion relations of the lowest order mode propagating in the model soft pipe for four imposed air pressures $\Delta P = \bullet 0$ Pa, $\bullet 200$ Pa, $\bullet 490$ Pa and $\bullet 780$ Pa. The solid lines are theoretical predictions, whose transparency encodes the ratio $\text{Im}(k_x)/|k_x|$, for which the input stretch ratio λ_θ and curvature radius \bar{R} are obtained from the static problem. (b) Normalized strip deflection $\delta(z)/w_0$ and curvature $|\kappa(z)|w_0$ profiles computed for the same imposed air pressures as in (a).

vature experienced by the strip, that is to describe the static finite deformation. We obtain the deflection $\delta(z)$ within the framework of large deflections of thin plates. The detailed assumptions and solution to the static problem are provided in appendix B. We show in figure 5(b) the normalized midline deflection profiles, $\delta(z)/w_0$, corresponding to the values of ΔP imposed in the experiments of figure 5(a). From these profiles, we can determine the membrane stretch ratio $\lambda = \ell/w_0$, where ℓ is the length of the deformed strip mid-surface, and obtain the normalized curvature profiles $|\kappa(z)|w_0$ (right panel of figure 5b). The imposed pressure generates a non-constant curvature, which exhibits strong variations near the edges of the strip because of the clamped boundary condition.

Accounting for the intricate details of this complex deformed configuration would require finite element simulations. Instead, we propose to introduce a simpler equivalent geometry, in which we evidence how pre-stress affects the propagation of the first flexion mode. We consider a clamped cylindrical strip whose radius of curvature and azimuthal stretching depend on ΔP . We take the radius of curvature, denoted \bar{R} , as the average of the curvature profile obtained from the static problem in the central region (dashed lines in the right panel of figure 5b), and assume that the equivalent strip is ho-

mogeneously stretched in the azimuthal direction with stretch ratio $\lambda_\theta = \lambda$. In this simplified geometry, the deformation is homogeneous and we can solve the elastodynamics equation (1) with the modified elasticity tensor $\mathbf{C}^0(\lambda_\theta = \lambda, \omega)$, with boundary conditions of vanishing incremental normal traction, and vanishing incremental displacement at $r = \bar{R} \pm h/2$ and $\theta = \pm w/(2\bar{R})$, respectively. The dispersion relations of the lowest order out-of plane modes computed for the couples $(\lambda_\theta, \bar{R})$ determined from the static problem are displayed as solid lines in figure 5(a). Despite our strong modeling assumptions, the predictions are in excellent agreement with the experimental data (filled circles). The model quantitatively captures the real part of k_x , and we also observe a qualitative agreement for its imaginary part: waves are not detected when we expect a large attenuation (encoded in the transparency of the solid lines). We emphasize that, in the parameter range considered in this study, the observed dispersion depends significantly on both \bar{R} and λ_θ , as expected from scaling relations obtained for the indentation of pressurized soft shells [58, 59].

We have evidenced that transverse initial stretch and strip curvature both speed up the propagation of out-of-plane elastic waves. When applying a static pressure difference in the absence of water, these two effects combine through the deflection of strip, and we capture their interplay in an equivalent geometry that enables us to retrieve the propagation properties of the strip's first flexion mode. In the following, we investigate how the soft, pre-stressed strip couples to the fluid waveguide in the presence of water.

V. INFLUENCE OF WATER LOADING

Flexion waves propagating in the soft strip set the surrounding water in motion, thereby increasing the inertia of the coupled system. This added mass effect decreases the wave speed, as observed when comparing the experiments of sections III and IV (figures 2c and 5a). The volume of fluid set in motion can be described using a penetration length. Indeed, as flexural waves propagate much slower in the soft strip than pressure waves in the fluid ($V_f = 1500 \text{ m s}^{-1}$), we expect evanescent waves in the surrounding water. We distinguish two asymptotic regimes: (i) a short-wavelength regime when the penetration length is smaller than the waveguide depth w_0 , and (ii) a long-wavelength regime when the penetration length is larger than w_0 , where the finite size of the fluid conduit must be taken into account.

A. Short-wavelength regime

We first consider the $k_x w_0 \gg 1$ regime in which the dispersion relation is similar to that of the first flexion mode of the strip, as evidenced in figure 6(a) for the water filled conduit with $\Delta P = 0$. In this regime, we

assume that the strip is coupled to a semi-infinite water medium. Similarly as in section II, we model the presence of the surrounding fluid as a boundary condition to the solid domain. Unlike in the case of a plate or a cylinder [35], there is no general expression for the normal stress, leading us to use an approximate boundary condition to obtain the dispersion relation of the first flexion mode. We assume that the solution in the water domain corresponds to a plane wave, with wavevector \mathbf{k}_f . The acoustic pressure at the water-strip interface reads,

$$P'(k_x, y = -h/2, z, \omega) = \rho_f \omega^2 \frac{\mathbf{u} \cdot \mathbf{e}_y}{i \mathbf{k}_f \cdot \mathbf{e}_y}, \quad (5)$$

where we invoked the continuity of the normal displacement at the interface [62]. We use Snell's law to express the normal projection of the fluid wavevector at the interface $(\mathbf{k}_f \cdot \mathbf{e}_y)^2 = \omega^2/V_f^2 - k_x^2 - k_z^2$, and further simplify this expression to $(\mathbf{k}_f \cdot \mathbf{e}_y)^2 \approx -k_x^2$ as (i) for the first flexion mode in the short-wavelength limit $k_z^2 \ll k_x^2$, and (ii) the longitudinal wave velocity in the fluid is much larger than the speed of the flexion mode. This approximation evidences the presence of evanescent waves and equation (5) thus underlines that the surrounding fluid acts as an added mass as $P' \propto \rho_f \omega^2$. We implement this approximate boundary condition and represent the predicted dispersion relation for $\Delta P = 0$ Pa in figure 6(a) (solid line). Although the prediction satisfactorily captures the experimental dispersion relation shape for short-wavelengths (in the high k_x region), it is shifted downwards compared to the experimental data, suggesting that we overestimate the water loading. We attribute this mismatch to edge effects: we do not model the presence of the side walls of the fluid waveguide which would reduce the volume of fluid set in motion.

We further test the relevance of this approximate boundary condition in the presence of pre-stress. We compute predictions for each ΔP using the equivalent geometry introduced in section IV C, that of a curved, azimuthally stretched clamped strip, where λ_θ and \bar{R} are extracted from the static problem (solid lines in figure 6c). We find a good agreement between the experimental data and the short-wavelength predictions for all imposed ΔP by systematically multiplying the calculated k_x by a factor 0.93, validating the use of the approximate boundary condition.

B. Long-wavelength regime

In the long-wavelength limit, we observe the most remarkable feature of water loading. The finite size of the fluid domain leads to the hybridization between the fundamental mode of the fluid waveguide and the flexion mode of the strip, giving rise to a non dispersive behavior (inset of figure 6a). We highlight that, in this limit, waves propagate at a speed of a few meters per second, *i.e.* three orders of magnitude slower than pressure waves in a rigid waveguide. While the experiments of section

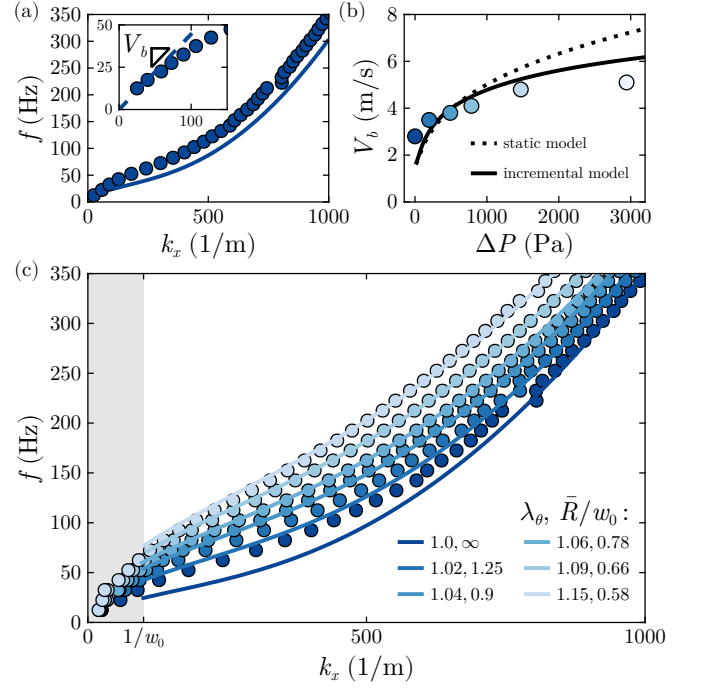


FIG. 6. (a) Dispersion relation in the water filled soft pipe for $\Delta P = 0$ Pa. In the long-wavelength limit, the propagation is not dispersive as evidenced by the dashed line in the inset, while for $k_x w_0 \gg 1$, the dispersion is similar to that predicted for a strip in contact with a semi-infinite fluid (solid line). (b) Velocity of the breathing mode V_b measured using a time of flight technique as a function of $\Delta P = \bullet 0$ Pa, $\bullet 200$ Pa, $\bullet 490$ Pa, $\bullet 780$ Pa, $\bullet 1500$ Pa, and $\bullet 2900$ Pa. (c) Dispersion relations in the water filled model soft pipe for all ΔP . The solid lines are predictions for the short-wavelength regime $k_x w_0 \gg 1$, which are fitted to the experimental data by multiplying all wavenumbers by a factor 0.93.

III (figure 2a) enable us to precisely measure the dispersion relation for $k_x w_0 > 1$, the inset of figure 6(a) evidences that the size of the experimental setup limits the resolution in k_x , preventing reliable measurements of the breathing mode velocity V_b . We thus perform complementary measurements to determine V_b using a time-of-flight approach. To increase the signal to noise ratio, we excite small amplitude waves with a one second long quadratic chirp signal with instantaneous frequency ranging from 1 Hz to 100 Hz, and obtain the impulse response by correlation of the measured displacement field $u_y(x, z, t)$ with the time reversed input signal. This response is then low-pass filtered, using a Butterworth filter with cutoff frequency of 6 Hz, to single out the non-dispersive regime. The wave speed is the slope of the propagating wavefront visualized in the spatiotemporal representation of the filtered impulse response. Figure 6(b) displays V_b for all imposed ΔP , where the slope angle is determined as the maximum of the Radon transform of the spatiotemporal (x, t) map. The wave velocity significantly increases with ΔP , underlining the influence of pre-stress in the long-wavelength regime.

We follow the same approach as when deriving the Moens-Korteweg velocity to obtain a prediction for V_b . Performing mass and momentum balances in the fluid contained in the soft conduit yields the speed of a pressure disturbance, $V_b = \sqrt{A/(\rho_f dA/d\Delta P)}$, where A is the cross-section of the fluid conduit. To estimate $dA/d\Delta P$, it is tempting to use the results of the static deflection problem by numerically integrating $\delta(z)$ along the conduit width, yielding the area $A(\Delta P)$ which we can then differentiate to get its variation with imposed pressure. The prediction obtained following this approach is represented with a dotted line in figure 6(b). While it qualitatively captures the increasing trend of V_b with the imposed pressure, it systematically and significantly overestimates the wave speed at large ΔP .

We address this shortcoming by introducing the following incremental approach, which recognizes that we excite small amplitude waves on top of a finite deformation. We consider the equivalent geometry of section IV C. Our goal is to obtain the deflection $\delta'(z)$ of the equivalent cylindrical clamped strip, with azimuthal stretch $\lambda(\Delta P)$ and radius of curvature $\bar{R}(\Delta P)$, upon applying an incremental pressure load P' . We derive an expression for $\delta'(z)$ using shallow shell theory [63], taking into account the background strip tension and the strip curvature but leaving out material non-linearities, as detailed in appendix C. We are thus able to numerically estimate the area increase in the deformed configuration $A' = \int \delta' dz$, and its variation with P' . In this incremental approach, the velocity V_b is given by,

$$V_b = \lim_{P' \rightarrow 0} \left(\sqrt{\frac{A}{\rho_f dA'/dP'}} \right). \quad (6)$$

This prediction, represented with a solid line in figure 6(b), is more consistent with our data, underlining the need to distinguish the reference and deformed configurations for large deformations. Yet, we still overestimate V_b at large ΔP , a discrepancy that could be attributed to our neglect of the material non-linearities although the stretch ratio remains small.

VI. CONCLUSION

We combine theory and experiments to investigate the propagation of guided waves in a model artery with the aim to assess the link between the wave speed and the properties of the arterial wall. We first obtain numerically the dispersion relation of low frequency guided waves propagating in soft elastic pipes filled and surrounded by water, and focus on the fundamental breathing and flexion modes that have been observed *in vivo* [16]. We identify two key pieces of information relevant to medical diagnosis. (i) In the frequency range of interest for shear wave elastography, both modes are dispersive, indicating that wave guiding must be taken into account to infer the wall elasticity, in agreement with literature

for the breathing mode. (ii) The flexural pulse wave velocity is highly sensitive to the pipe's surrounding, an effect we quantitatively capture in a long-wavelength model, making it less suitable than the breathing pulse wave to determine the arterial wall properties.

We then build a minimal artery phantom which reproduces the physics of the breathing mode. We explore the influence of pre-stress by varying the internal pressure, and observe that out-of-plane waves are sensitive to the imposed pressure both in the long-wavelength regime relevant to pulse wave propagation, and in the short-wavelength regime relevant to shear wave elastography. By singling out their contribution in dedicated experiments, we show how transversal stretching and curvature-induced rigidity combine to stiffen the pressurized phantom through the deflection of the soft wall. This approach allows us to develop a semi-analytical model, based on the acoustoelastic theory, that quantitatively captures the influence of imposed pressure on the breathing mode.

Finally, we discuss the coupling with the fluid waveguide by identifying the added mass associated to fluid motion in the limiting cases of small and large wavelengths. We draw a parallel between the low-wavenumber non-dispersive behavior in our experiments, stemming from the hybridization between fluid pressure waves and the first flexion mode of the clamped strip, and the pulse wave velocity. This enables us to show how the Moens-Korteweg formula can be reframed using an incremental approach in the presence of pre-stress. Interestingly, we find in our experiments that the low-wavenumber breathing wave velocity V_b increases with the imposed pressure ΔP , as reported for the arterial pulse wave velocity *in vivo* [18–20]. These observations seemingly contrast with predictions from the Moens-Korteweg formula (3), which associates an increase of ΔP to a decrease of the pulse wave velocity through an increase of tube radius and a decrease of wall thickness. This apparent discrepancy is resolved in the case of arteries, by acknowledging that equation (3) involves the incremental Young modulus [23]. In the physiological pressure range, the arterial wall exhibits a strongly non-linear behavior, becoming stiffer at larger transmural pressures, an effect that overcomes the velocity decrease predicted when considering only the geometrical variation of the artery with pressure. In our phantom, the increase of V_b with ΔP is instead tied to curvature-induced rigidity and background tension, reproducing the *in vivo* behavior but not its underlying cause.

To conclude, we evidence that quantitative predictions of wave propagation in the artery phantom require to take into account wave guiding, geometrical non-linearities, material non-linearities and their interplay with viscoelastic material properties. These results emphasize that pulse wave velocity and elastography measurements should always be analyzed in light of the applied pre-stress, and pave the way for imaging techniques that go beyond the determination of incremental elastic

moduli. These findings also suggest to investigate and model the influence of other forms of pre-stress acting on arteries, such as axial extension or stresses induced by tissue growth. Going further, studying the combined influence of pressure loading and axial stretching on the propagation of elastic waves in soft tubes could enable to predict the occurrence of bulging bifurcations, that is the possible formation of aneurysms [27, 64]. Finally, we expect blood flow to influence the propagation of arterial waves [18], an effect that the experimental setup developed in this work will enable us to probe.

ACKNOWLEDGEMENTS

We thank D. A. Kiefer for his help in implementing the spectral collocation method. This work has been partially supported by the Simons Foundation/Collaboration on Symmetry-Driven Extreme Wave Phenomena and received support under the program “Investissements d’Avenir” by the French Government.

Appendix A: Mooney-Rivlin model and modified viscoacoustoelastic tensor

We describe the behavior of Ecoflex OO-30 using the compressible Mooney-Rivlin model. The hyperelastic constitutive law relies on the strain energy density function W which is built on the principal invariants of the left Cauchy-Green tensor $\mathbf{B} = \mathbf{F} \cdot \mathbf{F}^T$,

$$W = \frac{\mu_0}{2} \left[(1 - \alpha) \left(\frac{I_1}{J^{2/3}} - 3 \right) + \alpha \left(\frac{I_2}{J^{4/3}} - 3 \right) \right] + \frac{\kappa}{2} (J - 1)^2, \quad (\text{A1})$$

with,

$$\begin{aligned} I_1 &= \text{tr}(\mathbf{B}) = \lambda_1^2 + \lambda_2^2 + \lambda_3^2, \\ I_2 &= \frac{1}{2} (\text{Tr}(\mathbf{B})^2 - \text{Tr}(\mathbf{B}^2)) = \lambda_2^2 \lambda_3^2 + \lambda_1^2 \lambda_3^2 + \lambda_1^2 \lambda_2^2, \\ I_3 &= \det(\mathbf{B}) = \lambda_1^2 \lambda_2^2 \lambda_3^2 = J^2, \\ \kappa &= \rho_s V_L^2. \end{aligned}$$

From W , an incremental approach allows to build a modified elasticity tensor $\mathbf{C}^0(\lambda_1, \lambda_2, \lambda_3)$ which describes the material response to small displacements superposed on the large deformation described by \mathbf{F} [53, 54]. The coefficients of \mathbf{C}^0 are given in [49] and are identical to that given in [53, 54] with a permutation of the last two indices.

The effect of viscoelasticity is also incorporated in the modified elasticity tensor \mathbf{C}^0 which now becomes fre-

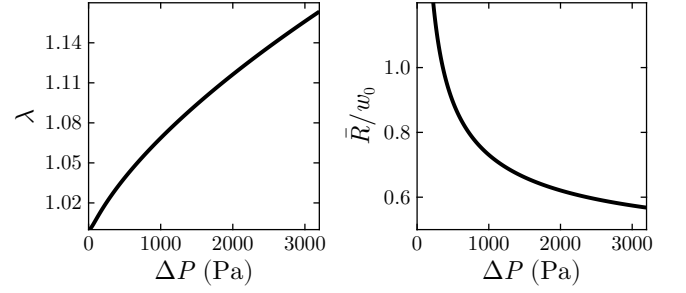


FIG. 7. Membrane stretch ratio $\lambda = \ell/w_0$ and normalized average central curvature \bar{R}/w_0 as a function of ΔP .

quency dependent and reads,

$$C_{jkl}^0(\lambda_1, \lambda_2, \lambda_3, \omega) = C_{jkl}^0(\lambda_1, \lambda_2, \lambda_3) + \mu_0 I_{jkl} \left(1 + \beta' \frac{\lambda_i^2 + \lambda_j^2 - 2}{2} \right) (i\omega\tau)^n, \quad (\text{A2})$$

with $I_{jkl} = (\delta_{jk}\delta_{il} + \delta_{jl}\delta_{ik})$, and $\beta' = 0.29$ for our soft elastomer [55]. The second term, that involves both the principal stretches and the frequency, underlines the coupling between pre-stress and viscoelasticity.

Appendix B: Static deflection

We consider the static deflection δ of a rectangular plate with a large aspect ratio clamped along its long edges and loaded with an imposed pressure ΔP , as sketched in figure 1(a). We look for solutions that are invariant along the x direction under the assumptions that the plate is thin ($h_0 \ll w_0$), that the deflection can be large ($\delta > h_0$), and that the strain remains small ($\delta \ll w_0$). With these hypothesis, the deflection $\delta(z)$ obeys the Föppl-von Kármán equation [65],

$$\frac{E_s h_0^3}{12(1-\nu^2)} \frac{d^4 \delta}{dz^4} - h_0 \frac{\partial}{\partial x_i} \left(\sigma_{zi} \frac{d\delta}{dz} \right) = \Delta P, \quad (\text{B1})$$

with clamped boundary conditions,

$$\begin{aligned} \delta(z = \pm w_0/2) &= 0 \\ \frac{d\delta}{dz} \Big|_{z=\pm w_0/2} &= 0, \end{aligned} \quad (\text{B2})$$

where ν is the Poisson ratio and $\boldsymbol{\sigma}$ is the Cauchy stress tensor. Equation (B1) can be simplified by realizing that the stresses σ_{zy} , and σ_{zz} do not vary significantly across the small thickness of the strip. From the boundary conditions, we obtain $\sigma_{zy} = 0$ and $\sigma_{zz} = T/h_0$, where T is the unknown membrane tension, so that (B1) becomes,

$$\frac{E_s h_0^3}{12(1-\nu^2)} \frac{d^4 \delta}{dz^4} - T \frac{d^2 \delta}{dz^2} = \Delta P. \quad (\text{B3})$$

We note that equation (B3) takes a similar form as Euler’s Elastica [61].

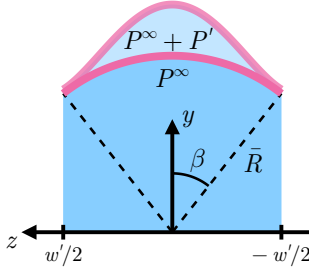


FIG. 8. Sketch of the equivalent strip geometry.

We determine the static deflection $\delta(z)$ as a solution of equation (B3) with boundary conditions given by (B2). The solution reads,

$$\delta = \frac{\Delta P w_0^2}{8T} \left[1 - \bar{z}^2 + \frac{2}{a} \left(\frac{\cosh(a\bar{z})}{\sinh(a)} - \coth(a) \right) \right], \quad (\text{B4})$$

where $a = w_0 \sqrt{T/B}/2$, $B = E_s h_0^3 / (12(1 - \nu^2))$, and $\bar{z} = 2z/w_0$. To obtain a prediction for δ , the next step is to elucidate the implicit dependence on the tension. This is achieved by computing the length of the deformed strip,

$$\ell = \frac{w_0}{2} \int_{-1}^1 \sqrt{1 + \left(\frac{d\delta}{d\bar{z}} \right)^2} d\bar{z}, \quad (\text{B5})$$

and by relating it to the tension using Hooke's law under a plane strain assumption,

$$T = \frac{E_s h_0}{1 - \nu^2} \left(\frac{\ell}{w_0} - 1 \right). \quad (\text{B6})$$

Combining equations (B4), (B5), and (B6) yields an equation that depends only on T and ΔP , enabling us to find T numerically when imposing ΔP . Having removed the implicit tension dependence, we proceed to get the deflection profile $\delta(z)$ from equation (B4), and the two quantities of interest for modelling wave propagation in the pressurized waveguide the membrane stretch ratio $\lambda = \ell/w_0$ and the normalized average central curvature \bar{R}/w_0 . We represent λ and \bar{R}/w_0 as a function of ΔP in figure 7. We note that, even for the largest imposed ΔP , λ remains in a range where we expect linear elasticity to hold from uniaxial traction test results [49], validating the use of the Föppl-von Kármán equations.

Appendix C: Equivalent strip model

We consider a cylindrical strip with radius of curvature \bar{R} , angular opening $2\beta = \lambda w_0/\bar{R}$, and thickness $h = h_0/\lambda$, where λ and \bar{R} are obtained from the static deflection problem, as sketched in figure 8. We model the deformation of this strip using the theory of shallow

shells [63]. We assume that the pre-stress in the strip is generated by a background pressure P^∞ , and are interested in the deformation when an incremental pressure P' is applied on top of the static load. We thus use a perturbative approach following [66, 67]. The equations of shallow shell theory in cartesian coordinates read,

$$\frac{E_s h^3}{12(1 - \nu^2)} \frac{d^4 \delta}{dz^4} + \frac{1}{\bar{R}} \frac{\partial^2 \phi}{\partial x^2} - \frac{\partial^2 \phi}{\partial x^2} \frac{d^2 \delta}{dz^2} = P^\infty + P' \quad (\text{C1})$$

$$\frac{\partial^4 \phi}{\partial z^4} + \frac{\partial^4 \phi}{\partial x^4} + 2 \frac{\partial^4 \phi}{\partial x^2 \partial z^2} = 0, \quad (\text{C2})$$

where ϕ is the Airy stress function which describes the middle surface stresses, and $\delta(z)$ is the displacement of the shell midline from its initial position $y \approx \bar{R} - z^2/(2\bar{R})$. The term $\partial_x^2 \phi / \bar{R}$ evidences the coupling between curvature and in-plane stretching responsible for the shell's geometric rigidity.

We first discuss the pre-stress generated by the static load. The imposed pressure induces membrane stresses,

$$T_{zz} = \frac{\partial^2 \phi^\infty}{\partial x^2}, \quad T_{xx} = \frac{\partial^2 \phi^\infty}{\partial z^2}, \quad \text{and} \quad T_{xz} = -\frac{\partial^2 \phi^\infty}{\partial x \partial z}, \quad (\text{C3})$$

where the Airy stress function ϕ^∞ is assumed to satisfy the biharmonic equation (C2) [66]. We follow the same approach as in section IV C and hypothesize that the equivalent circular strip is azimuthally stretched by λ , which amounts to setting the tension as $T_{zz}^\infty = 4/3 E_s h (\lambda - 1)$, and that the pre-stressed shape remains circular, that is δ^∞ is a constant. In doing so, we recover Laplace law from equation (C1), $T_{zz}^\infty = P^\infty \bar{R}$.

We now perturb this pre-stressed configuration by letting $\delta = \delta^\infty + \delta'$ and $\phi = \phi^\infty + \phi'$. At leading order, equation (C1) becomes,

$$\frac{E_s h^3}{12(1 - \nu^2)} \frac{d^4 \delta'}{dz^4} + \frac{T'_{zz}}{\bar{R}} - T_{zz}^\infty \frac{d^2 \delta'}{dz^2} = P', \quad (\text{C4})$$

where $T'_{zz} = \partial^2 \phi' / \partial x^2$ is an incremental tension. The solution to this equation with clamped boundary conditions for the incremental displacement at $z = \pm w'/2 = \pm \bar{R} \sin(\beta)$ is given by equation (B4) by letting $T \rightarrow T'_{zz}$, $\Delta P \rightarrow P' - T'_{zz}/\bar{R}$, and $w_0 \rightarrow w'$. Similarly as above, we elucidate the implicit dependence on the tension T'_{zz} by computing the length of the deformed shell midline and relating it to the tension using Hooke's law under a plane strain assumption, enabling us to find T'_{zz} , and thus $\delta'(z)$ when imposing P' . We then integrate δ' between $z = -w'/2$ and $z = w'/2$ when systematically varying P' , allowing us to numerically estimate the derivative dA'/dP' . As we use an incremental approach, the velocity V_b is given by equation (6).

We repeat this process for all couples (λ, \bar{R}) obtained from the static deflection problem, enabling us to compute V_b as a function of the imposed pressure ΔP , and thus to obtain a prediction for the wave velocity in the long-wavelength regime.

- [1] I. Levental, P. C. Georges, and P. A. Janmey, Soft biological materials and their impact on cell function, *Soft Matter* **3**, 299 (2007).
- [2] H. Yuan, S. Kononov, F. Cavalcante, K. R. Lutchen, E. P. Ingenito, and B. Suki, Effects of collagenase and elastase on the mechanical properties of lung tissue strips, *J. Appl. Physiol.* **89**, 3 (2000).
- [3] S. Kumar and V. M. Weaver, Mechanics, malignancy, and metastasis: the force journey of a tumor cell, *Cancer Metastasis Rev.* **28**, 113 (2009).
- [4] J. Bercoff, M. Tanter, and M. Fink, Supersonic shear imaging: a new technique for soft tissue elasticity mapping, *IEEE Trans. Ultrason. Ferroelectric. Freq. Control* **51**, 396 (2004).
- [5] R. M. S. Sigrist, J. Liau, A. El Kaffas, M. C. Chammas, and J. K. Willmann, Ultrasound elastography: review of techniques and clinical applications, *Theranostics* **7**, 1303 (2017).
- [6] W. P. Rogers, Elastic property measurement using rayleigh-lamb waves, *Res. Nondestr. Eval.* **6**, 185 (1995).
- [7] N. Bochud, J. Laurent, F. Bruno, D. Royer, and C. Prada, Towards real-time assessment of anisotropic plate properties using elastic guided waves, *The Journal of the Acoustical Society of America* **143**, 1138 (2018).
- [8] N. M. Shapiro, M. Campillo, L. Stehly, and M. H. Ritzwoller, High-resolution surface-wave tomography from ambient seismic noise, *Science* **307**, 1615 (2005).
- [9] Y. Ben-Shlomo, M. Spears, C. Boustred, M. May, S. G. Anderson, E. J. Benjamin, P. Boutouyrie, J. Cameron, C.-H. Chen, J. K. Cruickshank, *et al.*, Aortic pulse wave velocity improves cardiovascular event prediction: an individual participant meta-analysis of prospective observational data from 17,635 subjects, *J. Am. Coll. Cardiol.* **63**, 636 (2014).
- [10] M. E. Safar, Arterial stiffness as a risk factor for clinical hypertension, *Nat. Rev. Cardiol.* **15**, 97 (2018).
- [11] T. Young, I. the croonian lecture. on the functions of the heart and arteries, *Philos. Trans. R. Soc.* , 1 (1809).
- [12] L. Engelen, J. Bossuyt, I. Ferreira, L. M. van Bortel, K. D. Reesink, P. Segers, C. D. Stehouwer, S. Laurent, P. Boutouyrie, R. V. for Arterial Measurements Collaboration, *et al.*, Reference values for local arterial stiffness. part a: carotid artery, *J. Hypertens.* **33**, 1981 (2015).
- [13] J. Bossuyt, L. Engelen, I. Ferreira, C. D. Stehouwer, P. Boutouyrie, S. Laurent, P. Segers, K. Reesink, L. M. Van Bortel, R. V. for Arterial Measurements Collaboration, *et al.*, Reference values for local arterial stiffness. part b: femoral artery, *J. Hypertens.* **33**, 1997 (2015).
- [14] A. Moens, *Die pulscurve* (Leiden, 1878).
- [15] D. J. Korteweg, Ueber die fortpflanzungsgeschwindigkeit des schalles in elastischen rohren, *Annalen der Physik und Chemie* **5**, 525 (1878).
- [16] G. Laloy-Borgna, L. Puyo, H. Nishino, M. Atlan, and S. Catheline, Observation of natural flexural pulse waves in retinal and carotid arteries for wall elasticity estimation, *Sci. Adv.* **9**, eadf1783 (2023).
- [17] S. Gregoire, G. Laloy-Borgna, J. Aichele, F. Lemoult, and S. Catheline, Flexural pulse wave velocity in blood vessels, *J. Acoust. Soc. Am.* **155**, 2948 (2024).
- [18] M. B. Hstand and M. Anliker, Influence of flow and pressure on wave propagation in the canine aorta, *Circulation research* **32**, 524 (1973).
- [19] L. Marais, M. Pernot, H. Khettab, M. Tanter, E. Messas, M. Zidi, S. Laurent, and P. Boutouyrie, Arterial stiffness assessment by shear wave elastography and ultrafast pulse wave imaging: comparison with reference techniques in normotensives and hypertensives, *Ultrasound Med. Biol.* **45**, 758 (2018).
- [20] J. Baranger, O. Villemain, G. Goudot, A. Dizeux, H. Le Blay, T. Mirault, E. Messas, M. Pernot, and M. Tanter, The fundamental mechanisms of the korotkoff sounds generation, *Sci. Adv.* **9**, eadi4252 (2023).
- [21] M. Couade, M. Pernot, C. Prada, E. Messas, J. Emerich, P. Bruneval, A. Criton, M. Fink, and M. Tanter, Quantitative assessment of arterial wall biomechanical properties using shear wave imaging, *Ultrasound Med. Biol.* **36**, 1662 (2010).
- [22] G.-Y. Li, Q. He, R. Mangan, G. Xu, C. Mo, J. Luo, M. Destrade, and Y. Cao, Guided waves in pre-stressed hyperelastic plates and tubes: Application to the ultrasound elastography of thin-walled soft materials, *J. Mech. Phys. Solids* **102**, 67 (2017).
- [23] T. J. Pedley, *The Fluid Mechanics of Large Blood Vessels*, Cambridge Monographs on Mechanics (Cambridge University Press, 1980).
- [24] M. Bernal, I. Nenadic, M. W. Urban, and J. F. Greenleaf, Material property estimation for tubes and arteries using ultrasound radiation force and analysis of propagating modes, *J. Acoust. Soc. Am.* **129**, 1344 (2011).
- [25] E. Maksuti, E. Widman, D. Larsson, M. W. Urban, M. Larsson, and A. Bjällmark, Arterial stiffness estimation by shear wave elastography: validation in phantoms with mechanical testing, *Ultrasound Med. Biol.* **42**, 308 (2016).
- [26] T. Roy, M. Urban, Y. Xu, J. Greenleaf, and M. N. Gurdatti, Multimodal guided wave inversion for arterial stiffness: methodology and validation in phantoms, *Phys. Med. Biol.* **66**, 115020 (2021).
- [27] D. M. Haughton and R. W. Ogden, Bifurcation of inflated circular cylinders of elastic material under axial loading—i. membrane theory for thin-walled tubes, *J. Mech. Phys. Solids* **27**, 179 (1979).
- [28] D. M. Haughton and R. W. Ogden, Bifurcation of inflated circular cylinders of elastic material under axial loading—ii. exact theory for thick-walled tubes, *J. Mech. Phys. Solids* **27**, 489 (1979).
- [29] G. A. Holzapfel and R. W. Ogden, Constitutive modelling of arteries, *Proc. R. Soc. A: Math. Phys. Eng. Sci.* **466**, 1551 (2010).
- [30] R. W. Ogden, Nonlinear continuum mechanics and modeling the elasticity of soft biological tissues with a focus on artery walls, in *Biomechanics: trends in modeling and simulation* (Springer, 2016) pp. 83–156.
- [31] G. D. C. Kuiken, Wave propagation in a thin-walled liquid-filled initially stressed tube, *J. Fluid Mech.* **141**, 289 (1984).
- [32] H. Demiray, Solitary waves in prestressed elastic tubes, *Bull. Math. Biol.* **58**, 939 (1996).
- [33] Y. B. Fu and A. Il'ichev, Solitary waves in fluid-filled elastic tubes: existence, persistence, and the role of axial displacement, *IMA J. Appl. Math.* **75**, 257 (2010).
- [34] M. C. Junger, Vibrations of elastic shells in a fluid

- medium and the associated radiation of sound, *J. Appl. Mech.* **19**, 439 (1952).
- [35] H. Gravenkamp, C. Birk, and C. Song, Numerical modeling of elastic waveguides coupled to infinite fluid media using exact boundary conditions, *Comput. Struct.* **141**, 36 (2014).
 - [36] H. H. Bleich and M. L. Baron, Free and forced vibrations of an infinitely long cylindrical shell in an infinite acoustic medium, *J. Appl. Mech.* **21**, 167 (1954).
 - [37] T. C. Lin and G. W. Morgan, Wave propagation through fluid contained in a cylindrical, elastic shell, *J. Acoust. Soc. Am.* **28**, 1165 (1956).
 - [38] G. B. Warburton, Vibration of a cylindrical shell in an acoustic medium, *J. Mech. Eng. Sci.* **3**, 69 (1961).
 - [39] A. Adamou and R. V. Craster, Spectral methods for modelling guided waves in elastic media, *J. Acoust. Soc. Am.* **116**, 1524 (2004).
 - [40] J. Shen, T. Tang, and L. Wang, *Spectral methods: algorithms, analysis and applications*, Vol. 41 (Springer Science & Business Media, 2011).
 - [41] D. A. Kiefer, *Elastodynamic quasi-guided waves for transit-time ultrasonic flow metering* (FAU University Press, 2022).
 - [42] D. A. Kiefer, *Gew dispersion script* (2024).
 - [43] P. Chantelot and D. A. Kiefer, *Wave propagation in a model artery: dispersion scripts* (2025).
 - [44] J. C. Bramwell and A. V. Hill, The velocity of pulse wave in man, *Proc. R. Soc. of Lond. Ser. B* **93**, 298 (1922).
 - [45] S. S. Chen and G. S. Rosenberg, Free vibrations of fluid-conveying cylindrical shells, *J. Eng. Ind.* **96**, 420 (1974).
 - [46] J. F. Doyle, *Wave propagation in structures* (Springer International Publishing, 2021).
 - [47] M. Mooney, A theory of large elastic deformation, *J. Appl. Phys.* **11**, 582 (1940).
 - [48] R. S. Rivlin, Large elastic deformations of isotropic materials iv. further developments of the general theory, *Philos. Trans. R. Soc. London. Ser. A* **241**, 379 (1948).
 - [49] A. Delory, D. A. Kiefer, M. Lanoy, A. Eddi, C. Prada, and F. Lemoult, Viscoelastic dynamics of a soft strip subject to a large deformation, *Soft Matter* **20**, 1983 (2024).
 - [50] E. Rolley, J. H. Snoeijer, and B. Andreotti, A flexible rheometer design to measure the visco-elastic response of soft solids over a wide range of frequency, *Rev. Sci. Instrum.* **90** (2019).
 - [51] S. P. Kearney, A. Khan, Z. Dai, and T. J. Royston, Dynamic viscoelastic models of human skin using optical elastography, *Phys. Med. Biol.* **60**, 6975 (2015).
 - [52] M. Lanoy, F. Lemoult, A. Eddi, and C. Prada, Dirac cones and chiral selection of elastic waves in a soft strip, *Proc. Natl. Acad. Sci. USA* **117**, 30186 (2020).
 - [53] R. W. Ogden, *Non-linear elastic deformations* (Dover Publications, 1997).
 - [54] M. Destrade and S. G., *Waves in nonlinear pre-stressed materials* (Springer Vienna, 2007).
 - [55] A. Delory, F. Lemoult, A. Eddi, and C. Prada, Guided elastic waves in a highly-stretched soft plate, *Extreme Mech. Lett.* **61**, 102018 (2023).
 - [56] S. Wildeman, Real-time quantitative schlieren imaging by fast fourier demodulation of a checkered backdrop, *Exp. Fluids* **59**, 97 (2018).
 - [57] E. Reissner, Stresses and small displacements of shallow spherical shells. ii, *J. Math. Phys.* **25**, 279 (1946).
 - [58] A. Lazarus, H. C. B. Florijn, and P. M. Reis, Geometry-induced rigidity in nonspherical pressurized elastic shells, *Phys. Rev. Lett.* **109**, 144301 (2012).
 - [59] D. Vella, A. Ajdari, A. Vaziri, and A. Boudaoud, Indentation of ellipsoidal and cylindrical elastic shells, *Phys. Rev. Lett.* **109**, 144302 (2012).
 - [60] D. A. Kiefer, A. Delory, and F. Lemoult, *Gew soft strip* (2024).
 - [61] B. Audoly and Y. Pomeau, *Elasticity and Geometry: From Hair Curls to the Non-linear Response of Shells* (Oxford University Press, 2010).
 - [62] D. A. Kiefer, M. Ponschab, S. J. Rupitsch, and M. Mayle, Calculating the full leaky lamb wave spectrum with exact fluid interaction, *J. Acoust. Soc. Am.* **145**, 3341 (2019).
 - [63] E. Ventsel and T. Krauthammer, *Thin Plates and Shells: Theory: Analysis, and Applications* (Marcel Dekker, New York, 2001).
 - [64] Z. Guo, S. Wang, and Y. Fu, Localized bulging of an inflated rubber tube with fixed ends, *Philos. Trans. R. Soc. A* **380**, 20210318 (2022).
 - [65] L. D. Landau and E. M. Lifshitz, *Theory of elasticity: volume 7*, Vol. 7 (Pergamon Press Ltd., 1970).
 - [66] J. G. Berry and E. Reissner, The effect of an internal compressible fluid column on the breathing vibrations of a thin pressurized cylindrical shell, *J. Aero. Sci.* **25**, 288 (1958).
 - [67] D. Vella, A. Ajdari, A. Vaziri, and A. Boudaoud, The indentation of pressurized elastic shells: from polymeric capsules to yeast cells, *J. R. Soc. Interface* **9**, 448 (2012).